PAPER • OPEN ACCESS

Transverse structure and energy deposition by a subTW femtosecond laser in air: from single filament to superfilament

New Journal of Physics
The open access journal at the forefront of physics

Deutsche Physikalische Gesellschaft DPG
IOP Institute of Physics

Published in partnership with: Deutsche Physikalische Gesellschaft and the Institute of Physics

OPEN ACCESS

RECEIVED
9 October 2018

REVISED
21 January 2019

ACCEPTED FOR PUBLICATION
4 February 2019

PUBLISHED
28 March 2019

PAPER

Transverse structure and energy deposition by a subTW femtosecond laser in air: from single filament to superfilament

D Pushkarev[1], E Mitina[1], D Shipilo[1,2], N Panov[1,2,3], D Uryupina[1], A Ushakov[1,4], R Volkov[1], A Karabutov[3], I Babushkin[5,6], A Demircan[5,6], U Morgner[5,6], O Kosareva[1,2,7] and A Savel'ev[1,2]

[1] Faculty of Physics, Lomonosov Moscow State University, Moscow, Russia
[2] Lebedev Physical Institute of Russian Academy of Sciences, Moscow, Russia
[3] International Laser Centre, Lomonosov Moscow State University, Moscow, Russia
[4] Prokhorov General Physics Institute of Russian Academy of Sciences, Moscow, Russia
[5] Institute for Quantum Optics, Leibniz Universität Hannover, Hannover, Germany
[6] Cluster of Excellence PhoenixD (Photonics, Optics, and Engineering – Innovation Across Disciplines), Hannover, Germany
[7] Institute of Modern Optics, Nankai University, Tianjin, People's Republic of China

E-mail: abst@physics.msu.ru

Keywords: femtosecond filamentation, volumetric and linear energy density, air, wideband acoustic detection, forward Maxwell equation with resolved driver of the field

Supplementary material for this article is available online

Abstract

We traced experimentally transition from a single air filament to the superfilament under action of powerful loosely focused (NA $\sim$ 0.0021) femtosecond beam. Two regimes were exploited with multifilament formation by artificial amplitude or intrinsic amplitude/phase front modulation of the beam having 10–60 critical powers P_{cr}. Transverse spatial structure and energy density in the filament were studied using wideband acoustic detection and beam mode imaging single shot techniques at different distances along the optical path. We showed that with intrinsic front modulation a single extremely long ionized channel is formed provided peak power P of the initial beam does not exceed $20P_{cr}$. Its volumetric energy density is ~1.5–3 times higher than in the single filament, while linear energy density is almost 10 times higher. Artificial amplitude modulation leads to formation of either a single long filament or two closely spaced filaments at the same initial conditions. Maximal volumetric energy density was the same in both cases and slightly less than without this modulation. A few closely spaced filaments are generated at higher peak powers P with volumetric and linear energy densities experiencing fast nonlinear increase with P. Highest linear energy density achieved was 600 μJ cm^{-1}, i.e. almost 100 times higher than that of the single filament with increase in energy 10 times only. The volumetric energy density also increases by a factor of 10 to ~800 mJ cm^{-3} proving huge increase in intensity and electron density that is characteristic feature of the superfilamentation. These findings were supported by the numerical simulations based on the Forward Maxwell equation with resolved driver of the field that showed superfilament splitting and confirmed energy densities estimated from the experimental data.

1. Introduction

Filamentation of ultrashort laser pulses in gases is intensively studied for almost 30 years (see review papers [1–3] and references therein). The light filament is created due to dynamic balance between the focusing Kerr nonlinearity and the de-focusing field ionization impacts if the beam peak power P exceeds critical power (in air $P_{cr} \sim$ 5–10 GW), while its length and start position depend on the geometrical focusing, chirp, etc [4–8]. Intensity inside a filament is clamped to ~5–15 $\times$ 10^{13} W cm^{-2} [9] and electron density during light propagation is limited to ~10^{16}–10^{17} cm^{-3} [10–12]. Tight focusing may lead to higher intensities and electron densities inside a filament [4], while multiple filaments appear if energy/peak power of a femtosecond pulse increase [13]. Here laser intensity and electron density inside a distinct filament are almost the same as in the single filament regime.

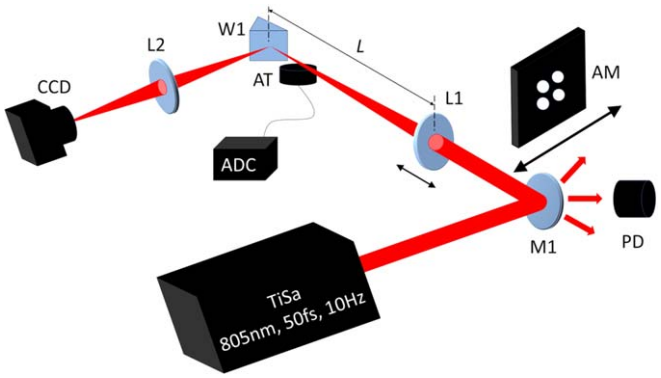

Figure 1. Experimental setup. M1–mirror, L1, L2–lenses, AT–acoustic transducer, W1–wedge, AM–amplitude mask.

Merging of several filaments into an extreme single filament event with drastically higher fluence has been observed in [5, 14], exhibiting the appearance of ubiquitous rogue wave phenomenon [14]. A special superfilamentation regime has been introduced recently [15] in which loosely focused femtosecond beam, having peak power well above the critical one, creates a bundle of filaments, stochastically merging in a superfilament near the geometrical focus. It was found that both linear energy deposition and electron density increase inside a superfilament [16]: at $F/30$ focusing the linear energy deposition rises 30 times than laser pulse energy E increases ~40 times (from a few mJ corresponding to the single filament regime). The energy range of $E \sim$ 5–20 mJ corresponds to creation and merging of a few filaments and here increase in the linear energy deposition was much steeper than at higher energies. Note, that there was no clear evidence that it was a single smooth superfilament that took the whole energy in [5, 15, 16].

First results on the fusion of a regularized four lobe beam produced with amplitude or phase mask was studied in [17, 18] both experimentally and numerically. It was shown, that four loosely focused beams merge before the focal point and a long single filament is formed with the amplitude mask while phase discontinuity created with a phase mask prevents filament merging. In [19] we reported preliminary data on the linear energy density of a filament formed from the four-lobe beam. We showed that this density increases much faster, almost quadratically, than the full energy of the initial beam.

This paper presents experimental data on 3D spatial and energy properties of merging filaments created by femtosecond subTW loosely focused beam with peak power P varied from 0.1 to 60 P_{cr}. First, we discussed data obtained with a regularized four lobe laser beam obtained with an amplitude mask, and then data from 'stochastic' filamentation is presented, where separate filament formation is governed by an intrinsic amplitude and phase modulation of the laser beam. Using beam mode imaging and wideband acoustic techniques we traced merging of a few separate filaments followed by a complex behavior and decay at different peak powers. The filament created at the highest peak powers up to 60 P_{cr} had very high energy density and can be treated as a superfilament. Our experimental findings are supported by numerical simulations based on the forward Maxwell equation (FME) with resolved driver of the field.

2. Experimental arrangement and methods

A TW Ti:Sa femtosecond laser system (805 nm, 50 fs, 10 Hz) was used in our experiments. Laser beam (0.8 cm FWHM) was loosely focused in air by the plane concave lens L1 with the focal distance $F = 312$ cm at 800 nm wavelength (see figure 1). The opaque plate AM with four closely spaced holes (4.2 mm in diameter each) was placed into the laser beam just before the lens thus creating a four-lobe beam. It causes twofold attenuation of the laser pulse energy. A calibrated photodiode PD monitors energy E after the lens by measuring scattered radiation from the mirror M1. This energy was controlled using halfwaveplate inserted into the beam before the compressor.

Two complementary methods were used to study transverse spatial structure and energy characteristics along a filament. First was imaging of the filament energy flow at a given distance from the lens. The wedge W1 was placed in the beam to slice out few percent of the laser pulse energy at a desired distance L from the lens. The wedge surface was imaged to the CCD (TheImagingSource dmk 23fv024) by the lens L2 to measure spatial energy distribution in its focal plane. The input surface of the wedge was damaged after a few laser shots. Hence the wedge was moved after each laser shot. To keep all the diagnostics within the same geometry and simplify

measurements procedures, the distance L from the focusing lens to the slicing wedge was changed by moving the lens along the optical axes.

To assess energy density inside a filament we used recently elaborated wideband acoustic detection technique [20]. An acoustic transducer AT (a 110 μm thick 6 mm in diameter polyvinylidene fluoride (PVDF) polymer film with working bandwidth up to 6 MHz) was placed 1 cm before the wedge 3–4 mm apart from the beam optical axis. The electronic signal from the transducer was digitized by the fast ADC (PLX9054 PCI PC card with digitization frequency 500 MHz, 8-bit resolution, Rudnev-Shilyaev Corporation) in each laser shot.

This setup allows to deduce both transverse spatial structure of a filament and energy density inside it from the acoustic signal. The transverse spatial resolution δx of this technique is linked to the minimum temporal width of the acoustic pulse $\tau_{\min}$, $x = c_{s\mathrm{T}\min}$, where c_s stands for the adiabatic sound velocity. The quantity $\tau_{\min}$ depends on the detector spectral bandwidth and air humidity. In [20] a simple model accounting for all impacts and well describing temporal form of an experimental acoustic signal from a femtosecond filament in air assuming a cylindrical heat source was presented and justified. The cylindrical Gaussian heat source $H(r,\ t) = H_0 \mathrm{e}^{-(r/w_0)^2}\delta(t)$ was used to estimate pressure signal $p(t)$ at the transducer. To evaluate the electrical signal from the piezoelectric transducer transmission coefficient of an acoustic wave at the air-PVDF interface $T = 2Z_{\mathrm{PVDF}}/(Z_{\mathrm{air}} + Z_{\mathrm{PVDF}}) \approx 2$ was used ($Z_{\mathrm{PVDF,air}} = \rho_{\mathrm{PVDF,air}} c_{s(\mathrm{PVDF}),s(\mathrm{air})}$ is the acoustic impedance with ρ stands for a density). For the PVDF piezoelectric film an electric signal in an idling mode $U(t) = g_{33}p(t)h$, where g_{33} is the voltage piezoelectric coefficient and h is the film thickness. Since the first critical angle of incidence of an acoustic wave at the air-PVDF interface is ~7.3°, only ~1.2 mm wide area of the 6 mm transducer effectively generates the electric signal. This determines also the longitudinal resolution of the acoustic technique.

Note, that two main impacts set the maximum volumetric energy density H_0 inside a filament—ion's energy stored due to ionization (proportional to the free electron density) and energy of molecular vibrational and rotational excitations [21]. If the filament-to-transducer distance is much larger than the initial energy deposition radius w_0, the analytical solution obtained for the forward problem of the optoacoustic tomography depends mainly on the H_0 and w_0 quantities. Thus, this model provides estimate for the beam radius w_0 (HWe^{-1} M) volumetric energy density H_0 and linear energy density along the filament ,$W = \pi H_0 w_0^2$ in each laser shot by fitting an experimental single shot acoustic trace. The linear energy density is also essential reflecting laser pulse losses along its optical path.

Test calculations showed that the width of a pulse obtained from the transducer is determined by three main impacts: the initial source radius w_0, the absorption coefficient α (mostly due to air humidity) and spectral response of the transducer. The minimal spatial resolution δx (at $w_0 = 0$) was assessed as ~50 μm in this experiment. So, we estimated the w_0 parameter first and then fitted the temporal envelope by adjusting the H_0 value for each acoustic trace.

The single filament regime was achieved in two ways: (i) without plate AM at $E \sim$ 2–3 mJ and (ii) with plate AM in the beam at $E \sim$ 10–20 mJ closing three holes of four in the plate. The fit gives $H_0 = 50 \pm 10$ mJ cm^{-3} and $w_0 = 60 \pm 10$ μm, or $W = 5 \pm 2$ μJ cm^{-1} (in perfect coincidence with previous data [22, 23]) for data obtained without the plate. An acoustic signal obtained in the single filament regime with AM inside the beam was one order of magnitude weaker and wider. Here the fit gives $H_0 = 15 \pm 5$ mJ cm^{-3} and $w_0 = 250 \pm 50$ μm, or $W = 30 \pm 5$ μJ cm^{-1}. This can be easily explained since focusing conditions were different: F/D ~ 400 and 1000 without the plate and with the plate in the beam respectively. Following data presented in [4] an electron density (that is proportional to the energy density per cubic cm) increases for a tighter focused beam, while the diameter of a filament decreases.

3. Experimental results and discussion

3.1. Filament merging with the amplitude mask

First, we checked beam transformation along the optical path in the small energy regime $E < 0.25$ mJ ($P \leqslant P_{\mathrm{cr}}$) with the amplitude mask inserted (figure 2, upper row). Each frame was obtained in a single shot. The beam preserves its four-lobe structure till the distance $L \sim 250$ cm, i.e. 60 cm before the geometrical focus of the lens (see the frame at $L = 240$ cm). Diffraction causes formation of the weak additional lobe in the center and some links between the initial lobes due to energy flow. The structure changes drastically at $L \sim 280$ cm. The four-lobe picture rotates by 45° and the central lobe becomes almost as bright as others. Near the geometrical focus, at $L = 290$ and 300 cm, and even after the focus at $L = 330$ cm the central lobe is the brightest one. The initial four-lobe picture restores at longer distances with low intensity lobe in the center. There were no acoustic signals from the transducer in this regime.

The beam profiles before the geometrical focus are well described by the simple diffraction integral (beam waist length is ~10–15 cm). These profiles close to the focal plane and after it are more complex since slight

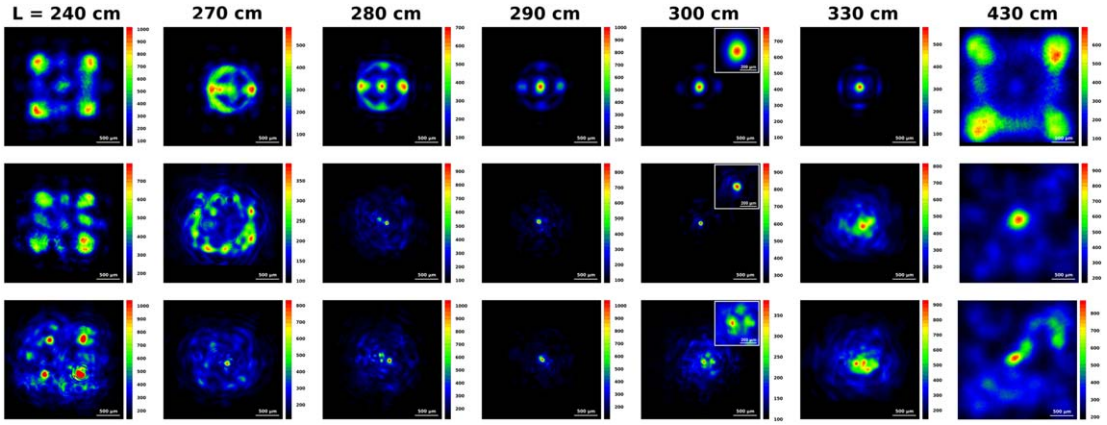

Figure 2. Spatial mode of a filament created with the four-hole amplitude mask at different distances L from the focusing lens for the laser pulse energy $E = 0.2$ mJ (upper row), 7 mJ (second row), 10–12 mJ (bottom row).

impact from the Kerr nonlinearity competes with diffraction: the B-integral acquired along the beam waist amounts to a few π in this regime.

Pictures obtained at higher energies $E \sim 6$–8 mJ ($P \sim 12$–$16\,P_{cr}$) are quite different (see figure 2, second row). Note, that peak power of ~15 P_{cr} should lead to formation of (in average) two to three distinct filaments in the freely propagation regime of filamentation [1]. Strong transverse energy flow is obvious at $L = 270$ cm already, while at $L > 280$ cm only the bright central spot survived due to a single filament formation. Those pictures are very like the picture, obtained in the single filament regime with three holes of four in the AM closed (not shown), but the minimum beam radius is smaller. This single spot picture preserves till $L \sim 330$ cm, and even al longer distances the beam profile with the central bright spot is still far from the initial four-lobe structure. Hence, filaments merge in a single exceptionally long filament in this regime.

Further increase in energy to $E \sim 10$–12 mJ causes filament breaking into a few after the focal area (see figure 2, bottom row). The number and brightness of individual filaments stochastically change from shot to shot, hence this row in figure 2 shows the most typical frames. Here energy passing through a single hole of the amplitude mask is enough to form a separate filament at $L \sim 240$ cm. Those filaments merge into one as early as at $L \sim 270$ cm with a huge energy reservoir around. This single filament breaks into a few due to additional energy flow from the reservoir and then refocusing forces the new spot-like filament at $L \sim 290$ cm with very weak reservoir around. This filament lasts for quite a long distance, but its cross section is quite complex (see figure 2, images at $L = 300$ and 330 cm, bottom row) and contains a few closely packed light channels united by a bright energy reservoir. Hence, we observed quite a complex picture that should be further considered from the energy density inside a filament assessed with acoustics data.

Figure 3 shows sample acoustic signals obtained at different positions along the optical path simultaneously with beam profiles (at the same distance L). A few-spike temporal structure of acoustics signals at $L < 270$ cm well corresponds to the beam profile frames. Amplitude of a spike was few times less than in the single filament regime. A huge single acoustic pulse was observed at $280 < L < 320$ cm. Its amplitude was ~5 times larger than that from a single filament without the amplitude mask and ~15 times larger than signals at $L < 270$ cm.

Figure 4(a) shows how the average amplitude of the acoustic signal depends on the distance L. A maximum amplitude is plotted here for $L < 270$ cm, where a few peaks were detected in the acoustic signal. One can see that at $L < 270$ cm this amplitude was the same as in the case of the single filament regime, but then it increases ~15 times and keeps almost constant at $280 < L < 320$ cm. Finally, it drops down to the amplitude corresponding to the standard single filament regime. Hence, the length of the filament with high energy density is almost 40 cm, and this is twice longer than the Rayleigh length.

Figure 4(b) gathers data on the radius of a filament. This radius abruptly drops to ~150 μm at $L \sim 270$ cm according to the acoustic data and then steadily increases till $L \sim 320$ cm, where the amplitude of an acoustic signal became too small to be used for fitting procedures. Note that radius of a filament w_0 strongly depends on the numerical aperture of the focusing lens [4], i.e. an initial laser beam diameter. Hence, we increased w_0 from 60 to 120–150 μm introducing the amplitude mask. The radius assessed from beam mode measurements is smaller (~120 μm) for $270 < L < 320$ cm. This can be explained from different origin of the two measurements: the beam mode measurement gets the instantaneous spot containing electromagnetic energy, while the acoustic detection reveals transversal size of the heat source created by the light. Note that this source is formed over few ns through ionization/recombination and molecular excitation relaxation [21]. The beam

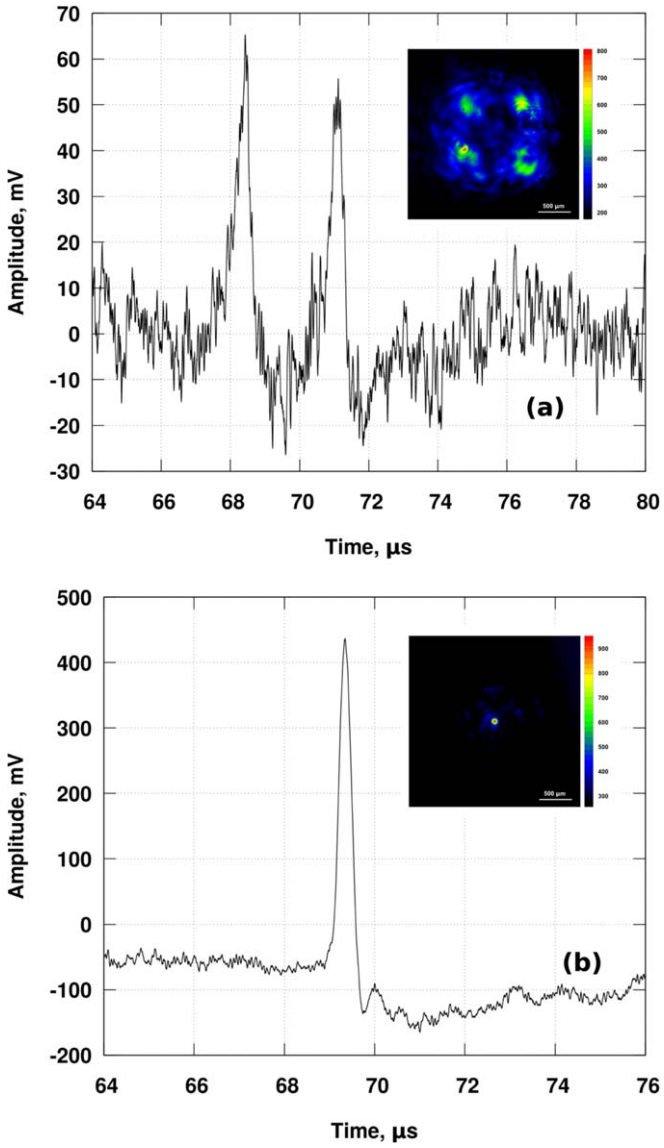

Figure 3. Acoustic signals and respective beam profiles (inserts) obtained in a single shot at $L \sim 260$ cm(a) and 300 cm (b) with the AM inserted ($E \sim 6$ mJ).

radius at longer distances, estimated from the beam mode measurement, grows slower than it is predicted by the diffraction theory due to the post-filamentation [24].

Figure 4(c) shows energy density inside the filament. It reveals two stages of the united filament formation: the filament formed at $270 < L < 290$ cm possesses high volumetric energy density (and this corresponds to the first merging event, see also figure 2 second and bottom rows at $L \sim 270$ cm), but its linear energy density is not high, while at $L \sim 290$ cm refocusing causes increase both in volumetric and linear energy densities. This lasts till $L \sim 310$ cm, that corresponds to the linear focus of the initial laser beam. Maximum linear energy density W is as high as 130 μJ cm^{-1} (compare to 5 μJ cm^{-1} for a single filament), while energy density per unit volume H_0 is 100 mJ cm^{-3} that is slightly higher than that for a single filament without the amplitude mask (60 mJ cm^{-3}). Increase in H_0 means twice higher electron density, that in its turn assumes intensity of laser radiation inside the united filament is higher than the clamping intensity [9]. Huge increase in W here is mainly due to larger radius of the united filament than the single filament's radius.

Note that at higher energies E this filament becomes more complex (see figure 2): one can see formation of a few closely packed filaments, well pronounced refocusing events, etc. Acoustic data shows that energy density is even higher here and increases with the energy E (see the next section).

3.2. Stochastic filamentation

In this part we will consider data obtained in the regime of 'stochastic' filamentation, where the peak laser power exceeds the critical one significantly ($P \sim 10$–$60\ P_c$), while multiple filamentation is governed by intrinsic

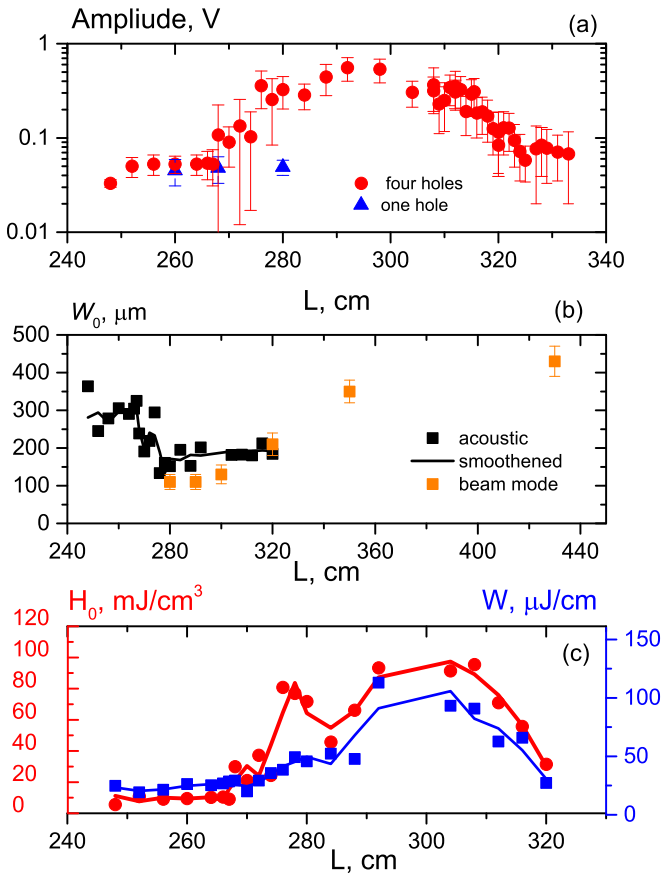

Figure 4. Amplitude of the acoustic signal (a), deduced acoustic source radius (b) and volumetric (red line and circles) and linear (blue line and squares) energy densities (c) dependences on the distance L from the focusing lens with amplitude mask inserted. $E \sim 10$ mJ. Figure 4(a) contains also data points (blue triangles) obtained with only one hole opened. Figure 4(b) contains data points (orange squares) obtained from the beam mode analysis, solid line was calculated as running average of the acoustic data.

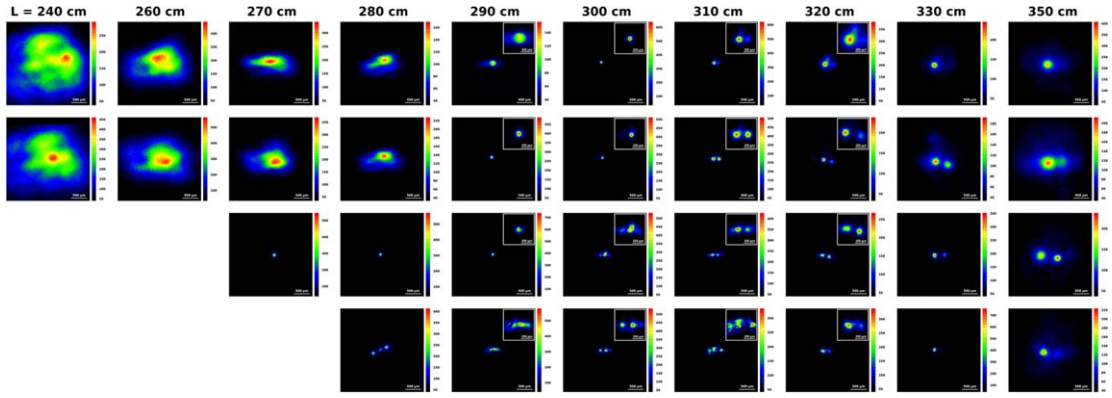

Figure 5. Spatial mode of a 'stochastic' filament at different distances L from the focusing lens for the laser pulse energy $E = 5$ (upper row), 8 (second row), 16 (third row) and 20 mJ (last row).

modulations of the laser beam amplitude (and/or phase) front. This study was done without any special amplitude mask before the focusing lens. The energy E changes from 0.2 to 30 mJ. We observed three distinct regimes of filamentation. At low energies $E < 3$ mJ a single filament was created (figure 5, upper row). It starts ~10 cm before the linear focus and lasts ~10–15 cm. Energy density inside this filament increases drastically with the pulse energy E (see below) and already at $E \sim 5$–8 mJ a united filament is formed (figure 5, second row) with carrying ~3 times higher energy density H_0. In most cases a single light channel is formed, but sometimes it breaks up into two. Only one filament survives due to energy dissipation at longer distances. The filament created at higher energies $E \sim 16$–20 mJ (figure 6, third and bottom rows) appears as early as at $L \sim 270$ cm,

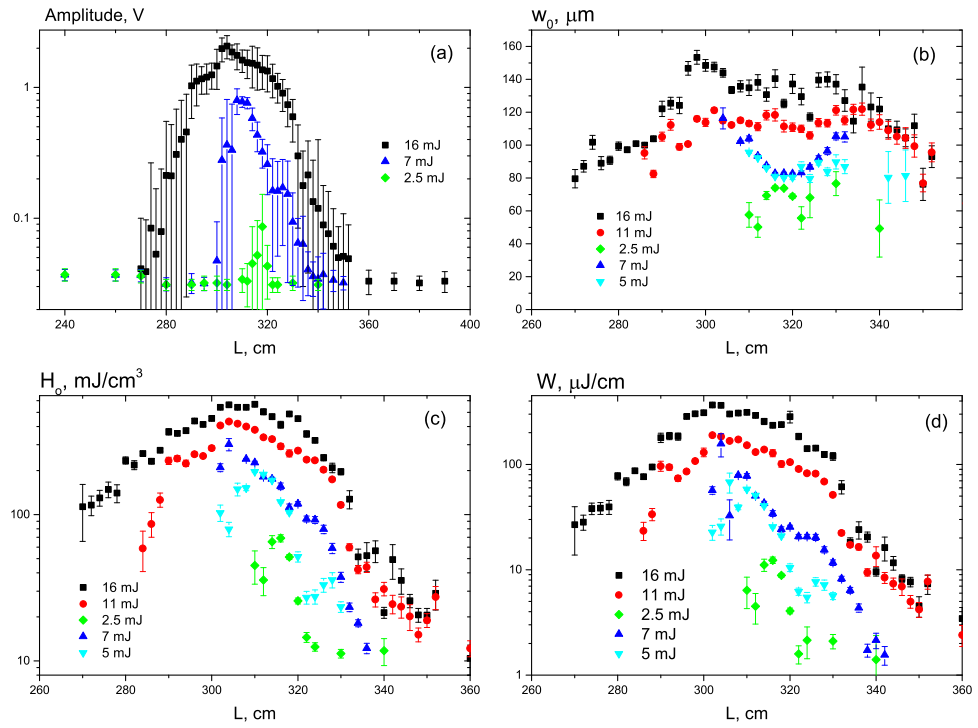

Figure 6. Amplitude of the acoustic signal (a), deduced acoustic source radius (b), volumetric (c) and linear (d) energy densities dependences on the distance L from the focusing lens in the stochastic filamentation regime for $E = 2.5$ (green dots), 5 (cyan dots), 7 (blue dots), 11 (red dots) and 16 mJ (black dots).

but it breaks up to a few closely packed filaments before the linear focus. Still, only one filament survives at longer distances L.

Figure 6(a) shows how an amplitude of acoustic signal changes with distance L at three characteristic energies E of 2.5, 7, and 16 mJ. A single filament is formed near the linear focus for $E = 2.5$ mJ, while at higher energies—well before. Data plotted in figures 6(b)–(d) was calculated from acoustic data. In the second regime of filamentation (5 and 7 mJ curves in figures 6(b)–(d)) the filament radius reaches its minimum at $L \sim 310$ cm, i.e. at the linear focus position, and is almost independent on the energy E. The density H_0 reaches its maximum earlier, almost at the beginning of the filament, and this depends on the energy E: maximum is located closer to the focusing lens for higher energies. The energy density decreased after the maximum and does not depend on the energy E for $L \sim 310$–320 cm. The same is valid for the linear energy density. It is worth mention that both volumetric and linear energy densities increased very fast with energy (see curves for a small E). Hence this second regime of stochastic filamentation corresponds to the formation of the united filament as in the previous section, but density H_0 is even higher due to smaller w_0.

The filament becomes much longer with further increase in the energy E. It starts at $L \sim 290$ and 270 cm for energies of 10 and 15 mJ. For the highest energy of 16 mJ the radius w_0 at $L \sim 270$–290 cm is almost constant and equal to that at lower energies (in the second regime). Growth in the w_0 from 100 to 140 μm at $L \sim 290$–300 cm is due to formation of an additional closely spaced filament. Obvious oscillations of the w_0 can be due to some refocusing and energy exchange between filaments. Volumetric energy density increases with the energy E from 20 to 400 mJ cm^{-3} for $E = 2.5$ and 15 mJ respectively, i.e. plasma concentration rises 20 times. The linear energy density increases by two orders, from few uJ cm^{-1} to sub mJ cm^{-1} level, due to increase in the overall filament radius. Hence here we observed transition to the superfilament. Its length estimated from the energy density curves is around 40 cm (from 290 to 330 cm) at $E = 15$ mJ and 20 cm at $E = 7$ mJ.

3.3. Energy scalings in different regimes

Figure 7 presents data for energy scaling of w_0, H_0 and W parameters in different regimes of filamentation measured at distance L, where mode beam measurements showed united filament or a few closely spaced filaments. Each point in the graphs corresponds to a single shot acoustic measurement. The threshold for a single filament formation, $E_{th} \sim 2$ mJ, is clearly visible, especially from the $H_0(E)$ dependence at low energies E (figure 7(b)). The filament radius, as well H_0 and W densities exhibit weak increase with the energy E up to 7–8 mJ in the stochastic regime. The filament radius is larger if the AM is introduced. As it was mentioned above this is due to lower numerical aperture of initial four beams passed through the AM. The radius w_0 has huge

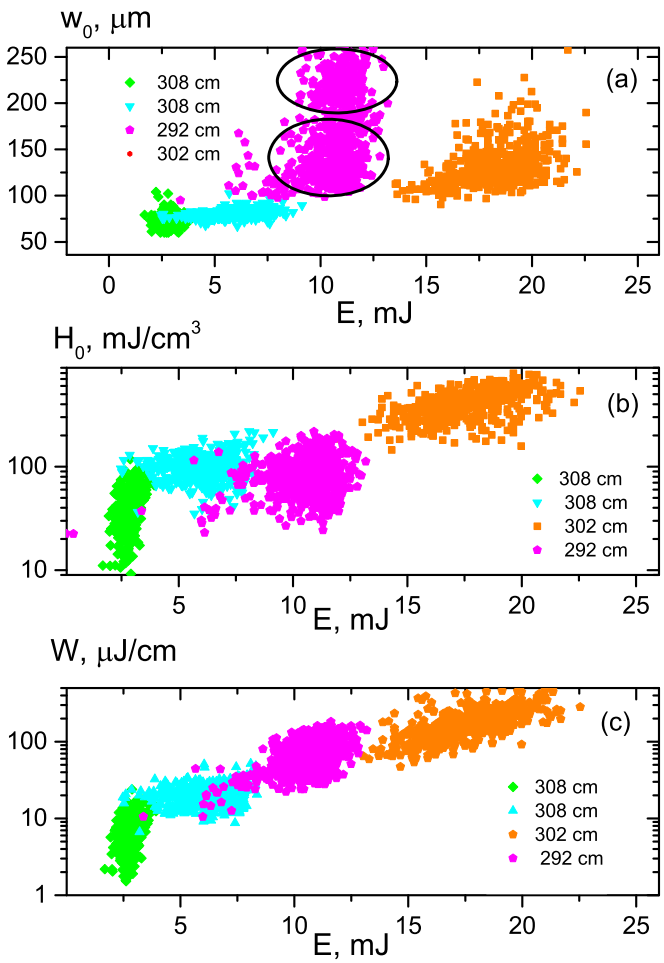

Figure 7. Deduced acoustic source radius (a), volumetric (b) and linear (c) energy densities dependences on the laser pulse energy E in different regimes of filamentation: single filament (green dots, 308 cm), strong filament (cyan dots, 308 cm), complex superfilament (orange dots, 302 cm) and with the four-hole amplitude mask (magenta dots, 292 cm).

scattering if the amplitude mask is inserted. Further analysis showed that there are two groups of data point in figure 7(a) in this regime with a single or double filament formation (shown with black circles). Note that the full energy of four beams after the AM is plotted in figure 7, hence energy in a single beam here is 2–4 mJ only.

The density H_0 of the united filament created with the amplitude mask (or by stochastic process at arbitrary low energies $E < 7$ mJ) is 1.5–3 times larger than that in a single filament regime (figure 7(b)). The 'threshold' of a single light channel breaking into a bundle of a few ones without the AM is $E \sim 8$–10 mJ, or $P \sim 20\,P_{cr}$ in our experimental configuration. This threshold seems much lower with the AM inserted: two groups of data points have almost the same mean energy E, while the H_0 density is the same, and coincides with the H_0 value for the stochastic data at $E < 8$ mJ. The linear energy density W experiences fast, nonlinear growth with the energy E (figure 7(c)). This dependence can be fitted with a linear function in the semi-logarithmic scale, except for a group of data points obtained with the amplitude mask. Here one group of data points satisfies the abovementioned 'linear' dependence, while for the second group linear density is much higher since the radius is almost twice larger.

Energies above 14–15 mJ ($P > 30\,P_{cr}$) are enough to create a superfilament. Arbitrary large radius scattering in figure 7(a) again is due to formation of a bundle of closely spaced filaments, but maximum volumetric energy shows fast growth with the energy, $E^{1.5}$ (figure 7(b)), that is related to huge increase both in the laser field intensity and electron density. The linear energy density W increases even faster as E^3 (figure 7(c)), because of simultaneous increase in the superfilament radius as $E^{0.8}$.

3.4. Numerical simulations

Formation of a few filaments in the superfilamentation zone with huge linear energy density for the pulse power of ~20 P_{cr} and higher (figures 2, 5) was observed for the first time. Hence, its reproduction in the numerical simulations is an excellent test for the modern filamentation paradigm. Numerical simulations were based on the FME [25, 26] with the resolved driver of the field using the solver in the (x, y, z, t) domain described in [17].

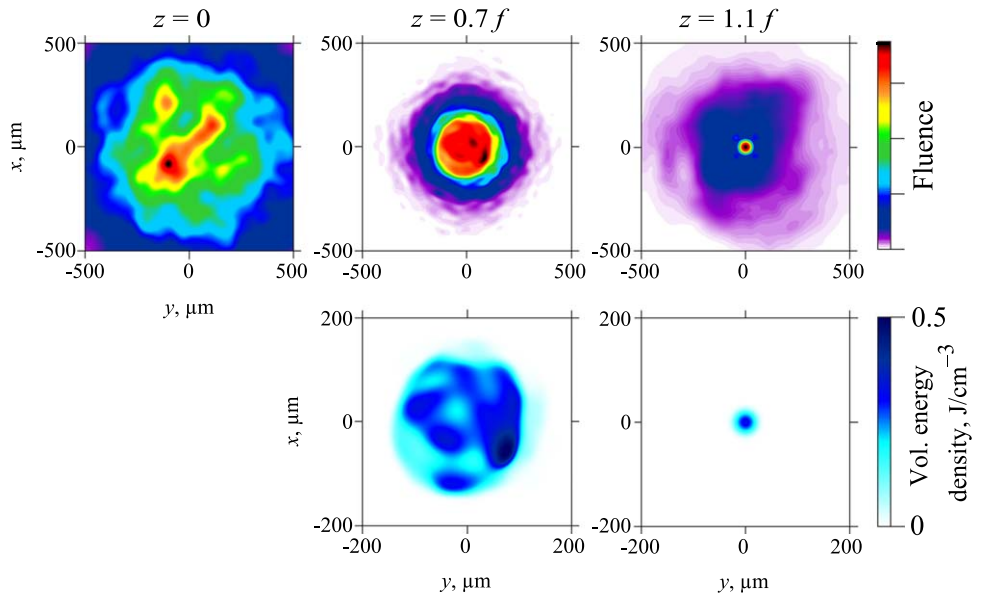

Figure 8. Transversal distributions of energy fluence (top row) and plasma density N_e (bottom row) at different propagation distances z/f. Ambient air density N_0 is 2.7 $\times$ 10^{19} cm^{-3}.

We performed simulations in the stochastic case: the spatial distribution of the field $E(t, x, y, z = 0)$ at the focusing lens was chosen as stochastically perturbed Gaussian:

$$E(t, x, y, z = 0) = E_0 \exp\left(-\frac{x^2 + y^2}{2a_0^2}\right) \times [1 + \xi(x, y)] \times e^{-t^2/2\tau_0^2} \cos\left[\omega_0 t + \frac{k_0(x^2 + y^2)}{2f}\right].$$

Here ω_0 and k_0 are the driver frequency and wavenumber corresponding to the wavelength of 800 nm, $2a_0 = 0.5$ mm is the beam diameter at the e^{-1} level, $2\tau_0 = 55$ fs is the pulse duration at the e^{-1} level, $f = 10$ cm is the geometrical focal length and the field amplitude E_0 corresponds to the pulse energy of 5 mJ, i.e. the pulse power of about 10 P_{cr}. The beam radius and focal length were chosen to have nearly the same numerical aperture in our calculation as in our experiments simultaneously making calculations easier. The noise $\xi(x, y)$ has the Gaussian autocorrelation function with the correlation radius of $0.1a_0$. The initial transversal distribution of the radiation fluence is shown in figure 8 at $z = 0$.

Plasma channels are formed at $z \approx 0.5f$, the maximal plasma density of 4 $\times$ 10^{17} cm^{-3} is achieved at $z = 0.7f$, i.e. before the geometrical focus. In the adequate agreement with the experiment the multi-string light and plasma structures are formed before the geometrical focus. These structures merge into the single filament after the geometrical focus: at $z = 1.1f$ the sole axially symmetrical filament survives.

Figure 9 shows how maximal intensity as well as volumetric and linear energy densities change with z (note logarithmic scale for the latter quantity). Energy densities were calculated from electron densities in the filament since our calculations did not include molecular excitations. The both energy densities have their maximal values at $z = 0.7f$. Absolute values are in reasonable agreement with experimental data. At longer distances (after the linear focus) the superfilament degrades into the single filament with 2–3 times lower volumetric energy density and linear energy density of a few μJ (see also cross sections in figure 8 at $z = 1.1f$). Thus, we reproduced numerically all stages of a superfilament formation and stagnation in reasonable quantitative agreement with the experimental data in figures 2–7.

4. Conclusions

Hence, our study sheds light onto transition from a single filament to the superfilament in air. We traced merging of a few separate filaments created under loose focusing of 5–60 critical power femtosecond beam. Two different regimes of initial filaments formation were used: (i) amplitude modulation with the special mask and (ii) stochastic filamentation from intrinsic amplitude and phase modulations. Volumetric and linear energy densities inside a filament were assessed using wideband acoustic detection of sound waves from the filament, while beam profile imaging along a filament provided additional visualization of the filament transverse spatial structure.

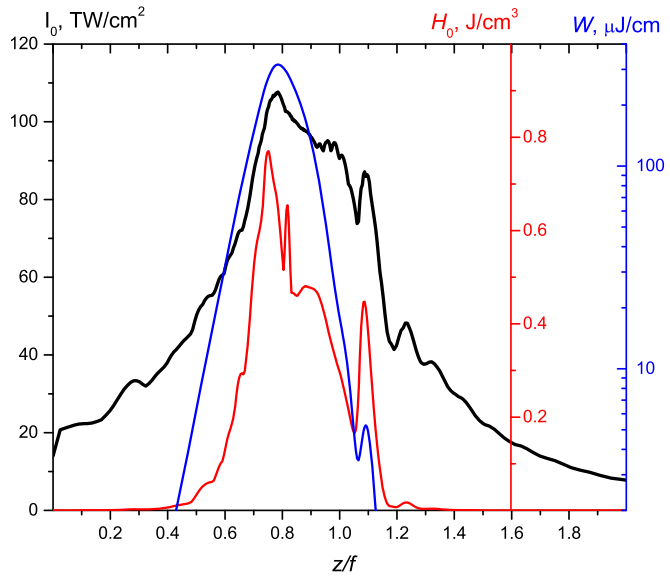

Figure 9. Simulated peak intensity I_0, volumetric energy density H_0 and linear energy density W dependence on the propagation distance z/f.

Nonlinear increase in the volumetric and linear energy densities inside a filament was observed in both regimes of filamentation. A single nice light channel can be formed before the linear focus due to a strong nonlinear interaction between separate filaments created by the amplitude mask. Its diameter is a larger than the diameter of a single filament created without the mask, while electron density inside the united filament exceeds density of a single filament 1.5–2 times. Bundle of a few separate closely spaced filaments can also be created in this regime with larger radius but almost the same maximal volumetric energy density. The linear energy density of the united filament increases from a few μJ cm^{-1} (an ordinary filament) to more than 100 μJ cm^{-1} here. This filament lasts for long distances and then gradually turned into an ordinary filament due to power dissipation.

The stochastic filamentation of the loosely focused beam exhibits different scenario. Here the volumetric energy density first sharply increased with the laser pulse energy E, and this corresponds to formation of a single filament with intensity clamping. The volumetric and linear energy densities experience weak increase with the energy E by a factor of 2–3. Hence the filament formed in this regime has higher laser intensity and electron density than a simple filament.

An additional closely spaced filament appeared if the peak power exceeds ~20 P_{cr}. Note, that onset of the multifilamentation of a freely propagating beam usually appears at lower peak powers of ~10 P_{cr}. Even more complicated transverse spatial structures were observed at higher peak powers with formation of a few closely spaced filaments. The volumetric and linear energy densities scale with peak power as $E^{1.5}$ and E^3 in this regime and reach as high as 800 mJ cm^{-3} and 400–600 μJ cm^{-1} respectively. That means huge increase in an electron density due to higher laser field intensity inside the filament, and this is the onset of the superfilamentation.

Complex spatial structure of a superfilament created at peak powers of 20 P_{cr} and higher should be considered for any special use. The results obtained are essential for modern applications of the superfilamentation regime such as terahertz generation, remote sensing and lasing, LIBS, discharge guiding, etc.

Acknowledgments

This work was supported by the Russian Science Foundation under grant #16-42-01060. The numerical model for stochastic superfilamtentation modeling was developed with support from Russian Foundation for Basic Research, grant 18-52-16020. I.B., A.D., and U.M. are thankful for the support by the DFG projects BA 4156/4-2 and MO 850-19/2 as well as Germany's Excellence Strategy within the Cluster of Excellence PhoenixD (EXC 2122, Project ID 390833453).

ORCID iDs

A Savel'ev https://orcid.org/0000-0002-1697-7487

References

[1] Chin S L, Hosseini S A, Liu W, Luo Q, Théberge F, Aközbek N, Becker A, Kandidov V P, Kosareva O G and Schroeder H 2005 The propagation of powerful femtosecond laser pulses in optical media: physics, applications, and new challenges *Can. J. Phys.* **83** 863

[2] Bergé L, Skupin S, Nuter R, Kasparian J and Wolf J-P 2007 Ultrashort filaments of light in weakly ionized, optically transparent media *Rep. Prog. Phys.* **70** 1633

[3] Couairon A and Mysyrowicz A 2007 Femtosecond filamentation in transparent media *Phys. Rep.* **441** 47

[4] Théberge F, Liu W, Simard P T, Becker A and Chin S L 2006 Plasma density inside a femtosecond laser filament in air: strong dependence on external focusing *Phys. Rev.* E **74** 036406

[5] Luo Q, Hosseini S A, Liu W, Gravel J-F, Kosareva O G, Panov N A, Aközbek N, Kandidov V P, Roy G and Chin S L 2005 Effect of beam diameter on the propagation of intense femtosecond laser pulses *Appl. Phys.* B **80** 35

[6] Golubtsov I S, Kandidov V P and Kosareva O G 2003 Initial phase modulation of a high-power femtosecond laser pulse as a tool for controlling its filamentation and generation of a supercontinuum in air *Quantum Electron.* **33** 525

[7] Mechain G, D'Amico C, Andre Y-B, Tzortzakis S, Franco M, Prade B, Mysyrowicz A, Couairon A, Salmon E and Sauerbrey R 2005 Range of plasma filaments created in air by a multi-terawatt femtosecond laser *Optics Commun.* **247** 171

[8] Durand M *et al* 2013 Kilometer range filamentation *Opt. Express* **21** 26836

[9] Kasparian J, Sauerbrey R and Chin S L 2000 The critical laser intensity of self-guided light filaments in air *Appl. Phys.* B **71** 877

[10] Tzortzakis S, Franco M, Andre Y-B, Chirton A, Lamouroux B, Prade B and Mysyrowicz A 1999 Formation of a conducting channel in air by self-guided femtosecond laser pulses *Phys. Rev.* E **60** R5305

[11] Bodrov S, Bukin V, Tsarev M, Murzanev A, Garnov S, Aleksandrov N and Stepanov A 2011 Plasma filament investigation by transverse optical interferometry and terahertz scattering *Opt. Express* **19** 6829

[12] Chen Y-H, Varma S, Antonsen T M and Milchberg H M 2010 Direct measurement of the electron density of extended femtosecond laser pulse-induced filaments *Phys. Rev. Lett.* **105** 215005

[13] Rodriguez M *et al* 2004 Kilometer-range nonlinear propagation of femtosecond laser pulses *Phys. Rev.* E **69** 036607

[14] Birkholz S, Nibbering E T J, Brée C, Skupin S, Demircan A, Genty G and Steinmeyer G 2013 Spatiotemporal rogue events in optical multiple filamentation *Phys. Rev. Lett.* **111** 243903

[15] Point G, Brelet Y, Houard A, Jukna V, Milian C, Carbonnel J, Liu Y, Couairon A and Mysyrowicz A 2014 Superfilamentation in air *Phys. Rev. Lett.* **112** 223902

[16] Point G, Thouin E, Mysyrowicz A and Houard A 2016 Energy deposition from focused terawatt laser pulses in air undergoing multifilamentation *Opt. Express* **24** 6271

[17] Shipilo D E, Panov N A, Sunchugasheva E S, Mokrousova D V, Andreeva V A, Kosareva O G, Seleznev L V, Savel'ev A B, Ionin A A and Chin S L 2016 Fusion of regularized femtosecond filaments in air: far field on-axis emission *Laser Phys. Lett.* **13** 116005

[18] Pushkarev D *et al* 2018 Effect of phase front modulation on the merging of multiple regularized femtosecond filaments *Laser Phys. Lett.* **15** 045402

[19] Pushkarev D, Mitina E, Uryupina D, Volkov R, Panov N, Karabutov A, Kosareva O and Savel'ev A 2017 Nonlinear increase in the energy input into a medium at the fusion of regularized femtosecond filaments *JETP Lett.* **106** 561

[20] Uryupina D, Bychkov A, Pushkarev D, Mitina E, Savel'ev A, Kosareva O, Panov N, Karabutov A and Cherepetskaya E 2016 Laser optoacoustic diagnostics of femtosecond filaments in air using wideband piezoelectric transducers *Laser Phys. Lett.* **13** 095401

[21] Tzortzakis S, Prade B, Franco M and Mysyrowicz A 2000 Time-evolution of the plasma channel at the trail of a self-guided IR femtosecond laser pulse in air *Opt. Commun.* **181** 123

[22] Jhajj N, Rosenthal E, Birnbaum R, Wahlstrand J and Milchberg H 2014 Demonstration of long-lived high-power optical waveguides in air *Phys. Rev.* X **4** 011027

[23] Rosenthal E, Jhajj N, Larkin I, Zahedrpup S, Wahlstrand J and Milchberg H 2016 Energy deposition of single femtosecond filaments in the atmosphere *Optics Lett.* **41** 3908

[24] Daigle J-F, Kosareva O, Panov N, Wang T-J, Hosseini S, Yuan S, Roy G and Chin S L 2011 Formation and evolution of intense, post-filamentation, ionization-free low divergence beams *Optics Commun.* **284** 3601

[25] Husakou A V and Herrmann J 2001 Supercontinuum generation of higher-order solitons by fission in photonic crystal fibers *Phys. Rev. Lett.* **87** 203901

[26] Kolesik M and Moloney J 2004 Nonlinear optical pulse propagation simulation: from Maxwell's to unidirectional equations *Phys. Rev.* E **70** 036604